Journal of Materials Chemistry A

ROYAL SOCIETY OF CHEMISTRY

PAPER

View Article Online
View Journal | View Issue

Cite this: J. Mater. Chem. A, 2023, 11, 22384

Fabrication of mesoporous nickel pyrophosphate electrodes and their transformation to nickel hydroxide with decent capacitance in alkaline media†

Işıl Ulu, [a] Burak Ulgut [a] and Ömer Dag *[ab]

The development of high-energy-density electrodes is paramount for the advancement of renewable and clean energy storage materials. In this study, we have devised a synthetic approach to fabricate mesoporous $Ni_2P_2O_7$ (*m*-NiPP) electrodes with a decent charge capacity. The method involves the formation of a liquid crystalline mesophase from an aqueous solution containing nickel nitrate hexahydrate salt (Ni(II)), pyrophosphoric acid (PPA), and a non-ionic surfactant (P123). The mesophase solidifies through the polymerization of Ni(II) ions and PPA, ultimately forming a mesostructured $Ni_2H_xP_2O_7(NO_3)_x{\cdot}nH_2O$ semi-solid, which can be subsequently calcined to yield mesoporous $Ni_2P_2O_7$ (*m*-NiPP). The gelation and polymerization process can be monitored using gravimetric, ATR-FTIR, XRD, and POM techniques as water evaporates during the transformation. The results reveal that the reaction between the Ni(II) ion and PPA initiates in the solution phase, continues in the gel phase, and concludes upon gentle heating. The same clear aqueous solution can be coated onto a substrate, such as FTO or graphite rods, and then calcined at various temperatures to produce the *m*-NiPP electrodes, composed of spherical mesoporous NiPP particles. These electrodes remain amorphous over a wide temperature range, but crystallize at approximately 700 °C while retaining their porous structure. However, when exposed to a 3 M KOH solution, the spherical *m*-NiPP particles undergo a transformation into β-$Ni(OH)_2$ particles. These transformed particles are approximately 1.5 nm thick, equivalent to 3–4 layers, and 7 nm wide, all while maintaining their spherical morphology. This transformation process occurs rapidly for amorphous *m*-NiPP and proceeds more slowly in the case of crystalline *m*-NiPP. The resulting electrodes exhibit a substantial charge capacity of 422 C g^{-1} and an impressive specific capacitance of over 1407 F g^{-1}.

Received 13th September 2023
Accepted 7th October 2023

DOI: 10.1039/d3ta05578g

rsc.li/materials-a

Introduction

Nano-porous transition metal phosphate (TMP) and pyrophosphate (TMPP) materials have recently been targeted for battery and supercapacitor applications.[1–11] However, there are only very few methods to produce mesoporous TMP or TMPP materials that can be synthesized by reacting transition metal ion(s) with phosphate or pyrophosphate ion(s), respectively.[12–17] These reactions are very fast and usually produce large TMP and TMPP particles that are difficult to self-assemble with surfactant micelles in aqueous or non-aqueous media. Recently, we have developed a new synthetic approach that uses an acid–salt-surfactant (acid is phosphoric acid (PA)[18,19] or pyrophosphoric acid (PPA)) lyotropic liquid crystalline (LLC) mesophases, where the reaction between metal and phosphate or pyrophosphate ions can be slowed down. The acid–salt-surfactant LLC mesophase forms with sufficiently high acid and salt concentrations upon almost complete evaporation of the water from a clear aqueous solution of the ingredients (transition metal salt (TMS), PA or PPA, and a non-ionic surfactant, namely Pluronic ($PEO_nPPO_mPEO_n$, PEO is the poly-ethylene oxide block and PPO is the poly-propylene oxide block) or oligo (ethylene oxide)). The TMS-PA (or PPA)-surfactant mesophase can be converted into a mesostructured solid TMP[19] and TMPPs upon slow polymerization reaction between the metal ions and PA or PPA species, respectively. The polymerization reaction starts in the aqueous solution, continuous during solvent evaporation (gelation process) and in the gel-phase. The gel-like semi-solid form of a spin- or dip-coated, or drop-casted sample can be calcined at as low as 300 °C (or higher temperatures) to obtain mesoporous TMP or TMPPs particles.

Porous $M_2P_2O_7$ materials display high capacitance as demonstrated by many research groups;[13–17,20–25] there is a common consensus that the $M_2P_2O_7$ transforms to

[a]Department of Chemistry, Bilkent University, 06800, Ankara, Turkey
[b]UNAM — National Nanotechnology Research Centre and Institute of Materials Science and Nanotechnology, Bilkent University, 06800, Ankara, Turkey. E-mail: dag@fen.bilkent.edu.tr

† Electronic supplementary information (ESI) available. See DOI: https://doi.org/10.1039/d3ta05578g

$M_2P_2O_7(OH)_2$ upon first oxidation (M^{2+} to M^{3+}) step and to $M_2P_2O_7(O)_2$ in further oxidation (M^{3+} to M^{4+}) step to display such a high capacitance.[24,25] For instance, the theoretical capacitance of $Ni_2P_2O_7$ can be as high as 662 F g^{-1} in the first oxidation step and doubles in the second. Kim and co-workers recorded a specific capacitance (SC) of 1893 F g^{-1} at 2 mA g^{-1} current density from a highly porous graphitic carbon/$Ni_2P_2O_7$ hybrid device.[25] Similarly, other transition metal pyrophosphates such as $Mn_2P_2O_7$ and $Co_2P_2O_7$ that are isostructural with $Ni_2P_2O_7$ should also have high SC, but $Mn_2P_2O_7$ (ref. 26) and $Co_2P_2O_7$ display relatively low SCs,[27] and therefore they are not as attractive as $Ni_2P_2O_7$. The main focus of this work is on the mesoporous $Ni_2P_2O_7$ electrodes because they display a significantly high SC performance. Note also that some nickel-containing mixed metal pyrophosphates, such as $Ni_{2-x}Co_xP_2O_7$, also show high SCs.[28,29] Even though these metal pyrophosphates have similar crystal structures and display very similar XRD patterns, they behave differently under similar electrochemical test conditions.

It is also important to mention that the metal pyrophosphate materials have been characterized very well to show that the starting materials are either amorphous or crystalline $M_2P_2O_7$.[12–29] However, the characterization of the used electrodes is relatively poor due to the difficulties of handling the used electrodes that are mainly fabricated by mixing metal pyrophosphate particles with many additives. Here, we show a novel synthetic method for fabricating the $Ni_2P_2O_7$ electrodes for the first time using the LLC approach over a graphite rod (GR) without any additives and its performance in electrochemical tests. The mesoporous $Ni_2P_2O_7$ (denoted as *m*-NiPP) electrodes were characterized using multi-analytical techniques in every step while cycling the electrodes in the potential range of −0.5 to 1.5 V *versus* Ag/AgCl. We found that the *m*-NiPP electrode transforms to an *m*-$Ni(OH)_2$ electrode upon immersing it into a 3 M KOH solution for a short time. Therefore, it is actually the *m*-$Ni(OH)_2$ electrode which is used in further electrochemical tests. This transformation is a new and unique way of producing *m*-$Ni(OH)_2$ electrode that has a high SC in alkali media and performs as a promising electrocatalyst for oxygen evolution reaction. Moreover, this investigation, for the first time, shows that the reported electrochemical properties (such as high SC, CV, and GCD curves) in the literature for the NiPP electrodes in alkali media originate from the layered $Ni(OH)_2$, not from the NiPP.

Note that there are two forms of layered nickel hydroxide (α- and β-$Ni(OH)_2$).[30–35] The α-$Ni(OH)_2$ is not stable in an alkaline media and transforms into the β-$Ni(OH)_2$.[34–39] Therefore, it is essential to synthesize β-$Ni(OH)_2$ with a reduced number of layers in each β-$Ni(OH)_2$ nanoparticles for a high SC.[32–40] Because the number of accessible Ni^{2+} on the surface becomes maximum in a two-layer β-$Ni(OH)_2$ with a theoretical capacity of 1040 C g^{-1} (2080 F g^{-1} in 0.5 V potential window) in the first electron transfer and doubles in case of two-electron process and decreases as a function of $2/n$ (where n is the number of layers in a particle) by increasing the number of layers. This work shows for the first time that the nickel pyrophosphate is not stable in an alkaline media and quickly transforms to nickel hydroxide in the form of very thin β-$Ni(OH)_2$ nano-flakes, as demonstrated using *m*-NiPP coated graphite rod electrodes and powder samples.

Results and discussion

Mesophase formation and its solidification

Clear aqueous solutions of nickel nitrate salt, pyrophosphoric acid (PPA), and surfactant (P123, $H(OCH_2CH_2)_{20}$-$(OCH(CH_3)CH_2)_{70}$-$(OCH_2CH_2)_{20}OH$) with a salt/acid mole ratio of 2 and salt/surfactant mole ratio of between 10 and 100 were prepared in 10 mL water. Then, the solutions are spin- or dip-coated, or drop-casted over substrates (such as FTOs, graphite rods, or microscope slides) and followed during the water evaporation process. The spin- and dip-coated sample quickly loses its water and turns into a lyotropic liquid crystalline mesophase (gel) that transforms into a semi-solid over time. In contrast, the drop-casted sample transforms in a much longer time, depending on the drop size. Note also that the above compositions were intentionally chosen, because the mesophase/mesostructured semi-solid phases are stable in these compositions.

Time-dependent aging/water evaporation was monitored using three different techniques (namely, ATR-FTIR, POM, and XRD). The process was also followed by gravimetric measurement by putting about 1 g of a solution and monitoring the change in weight of the sample under ambient conditions over a 4-digit balance; see Fig. S1, ESI.† The solution loses water monotonically, see the range I in Fig. S1, ESI,† and reaches a plateau upon completion of the water-lost. Clearly, there are 2 more steps (II and III) in the weight-lost plots due to a chemical reaction that produces more volatile species. Combining this information with the ATR-FTIR (attenuated total reflectance-Fourier transform infrared) spectra and polarized optical microscopy (POM) images recorded during water evaporation show that the nitrate species decompose as nitric acid and its decomposition products and are removed from the media (see later). Likely, the following reaction occurs during water evaporation and further steps.

$$2Ni(NO_3)_2 + H_4P_2O_7 + nH_2O \leftrightarrow Ni_2H_xP_2O_7(NO_3)_x\cdot nH_2O(s) + (4-x)HNO_3(g) \quad (1)$$

The aging process was also followed under a POM using various compositions from 10 : 5 : 1 to 90 : 45 : 1, Ni(II) : PPA : P123 mole ratios with an increment of 10 : 5 Ni(II) : PPA by drop casting over glass microscope slides. Fig. 1 shows two POM

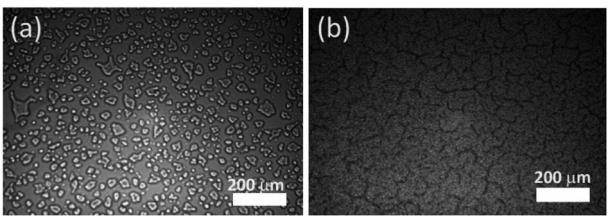

Fig. 1 POM images of (a) 10 : 5 : 1 and (b) 80 : 40 : 1, Ni(II) : PPA : P123 after 1 day aging/water evaporation (scale bars are 200 μm).

images from low (10 : 5) and high (80 : 40) concentrated samples after 1 day of aging. Fig. S2† displays the POM images, recorded at two different aging times (15 min and 1 day) of the samples with Ni(II) : PPA : P123 mole ratios of 10 : 5 : 1, 20 : 10 : 1, 40 : 20 : 1, and 80 : 40 : 1. The POM images display particle-like morphology due to solidification of the mesophase. The particle-like small domains are more in the highly concentrated compositions and less in the low concentrations, due to the formation of more solid $Ni_2H_xP_2O_7(NO_3)_x \cdot nH_2O$ particles (compare the images in Fig. 1). Clearly, solid particle formation starts in 15 minutes, enhances with increasing salt/P123 mole ratio, and covers the entire sample after 1 day of aging/water evaporation under ambient conditions. Aging of the spin-coated samples has also been followed using X-ray diffraction (XRD) to collect their time-dependent patterns at small and wide angles and to show the formation of mesophases and/or mesostructured solids and no crystallization of salt species, respectively.

Fig. 2 and S3, ESI,† show sets of XRD patterns of all compositions. At low Ni(II)/P123 mole ratios (10 to 40), the diffraction line at around 1.7°, 2θ, appears even in the freshly coated sample and remains during aging (except 10 mole ratio, in that the diffraction line disappears in 2 h aging). Note that the mesophase forms quickly by spin-coating the solutions over the glass slides. In the high Ni(II)/P123 mole ratios, the diffraction line appears in later aging time, indicating that the water evaporation takes much longer (see latter). The most intense line of the patterns must be below 1°, 2θ, and could not be measured by the current setup of our diffractometer, but in some samples, 3 lines, namely due to (200), (300), and (400) planes, are observed. The diffraction line(s) gradually shifts to higher angles with water evaporation and polymerization reactions (see latter). Note also that a sample of a 100 mole ratio also displays diffraction line(s) at small angles, indicating an ordered structure exists even at such high concentrations. However, it is difficult to identify the structural details of the mesophase or mesostructured semi-solid samples. If we assume the same structure forms in all compositions, the likely process is the formation of a mesophase with a reduced P123 concentration or reduced aggregation number in the mesophase.

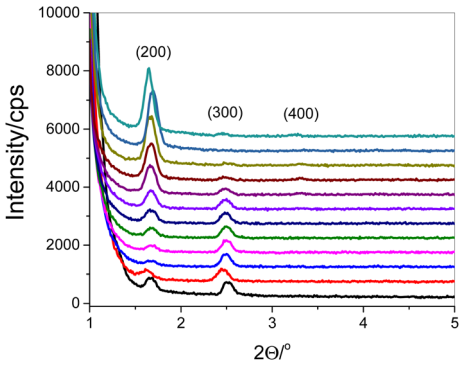

Fig. 2 Aging time-dependent (bottom to top, fresh, 10, 20, 30, 40, 50, 60, 90 min, 2, 3, 5, and 24 h) small-angle XRD pattern of Ni(II) : PPA : P123 mole ratios of 30 : 15 : 1.

Otherwise, one would expect a gradual shift of the diffraction line(s) to lower angles with increasing inorganic ingredients in the hydrophilic domains of the mesophase. Moreover, the inorganic ingredients (nickel nitrate and PPA) undergo polymerization reactions (see latter) in the mesophase that also cause a gradual contraction; as a result, the diffraction line(s) instead shifts to higher angles.

Note also that the drop size on the ATR crystal (Dimond, for IR measurements) and balance (for gravimetric measurements) is much thicker than those samples coated over microscope slides for POM images and XRD measurements. Therefore, gelation and solid particle formation start at different aging periods and can be monitored by all four techniques.

Three of the above solutions were chosen with a low (30 : 15 : 1, Ni(II) : PPA : P123) intermediate (60 : 30 : 1, Ni(II) : PPA : P123), and high (90 : 45 : 1, Ni(II) : PPA : P123) inorganic compositions, labelled as solutions A, B, and C, respectively. One drop of each clear solution was put on the ATR crystal (diamond) of the spectrometer, and the IR spectra were collected over time. Fig. S4, ESI,† shows a set of time-dependent ATR-FTIR spectra collected from those solutions. In all compositions, the peaks at 1640 and 3000–3600 cm^{-1} (due to water) and around 1290–1470 cm^{-1} (due to nitrate species) lose intensity; however, the peaks at about 800–1200 cm^{-1} (due to pyrophosphate species) gain intensity over time, indicating evaporation of water and nitrate species from the media, increasing of the concentration and refractive index of the sample, respectively.

It is important to note that the ATR-FTIR data must be handled carefully to get quantitative information and to compare spectra with each other. During the water evaporation process, both the concentration of the solution and depth of the evanescent wave (due to the increase of the refractive index of the sample, see Fig. S5(a), ESI†) increase, therefore both c and b increase in Beer's equation ($A = \varepsilon bc$, A is absorbance and measured, ε is the extinction coefficient and constant, b is the thickness, and c is the concentration). Also, note that the refractive index increases from 1.33 (in water) to 1.50 (in surfactant media).[41] It means the depth of the evanescent wave also increases by almost 2 times and depends on the wavelength of the incident beam; see Fig. S5(b), ESI,† and related information in the ESI section.† However, normalizing the spectra using either a surfactant or pyrophosphate peaks may overcome both issues because both ingredients (P123 and PPA) remain in the media during evaporation. The spectra are normalized to quantitatively follow the evaporation and chemical reactions during the aging process. Fig. 3(a) displays time-dependent normalized ATR-FTIR spectra from solution B (the other two compositions are given in Fig. S6(a and b), ESI†). The spectral features in the nitrate, water, and PPA regions (1280–1520, 1640/3000–3600, and 900–1100 cm^{-1}, respectively) change during water evaporation, indicating a polymerization and decomposition reactions occurring among the ingredients and resulting evaporation of water and volatile decomposition products.

In the raw spectra (Fig. S4, ESI†), the water peaks are quite suppressed due to the smaller refractive index (aqueous solution) in the early spectra. Therefore, the spectra are normalized

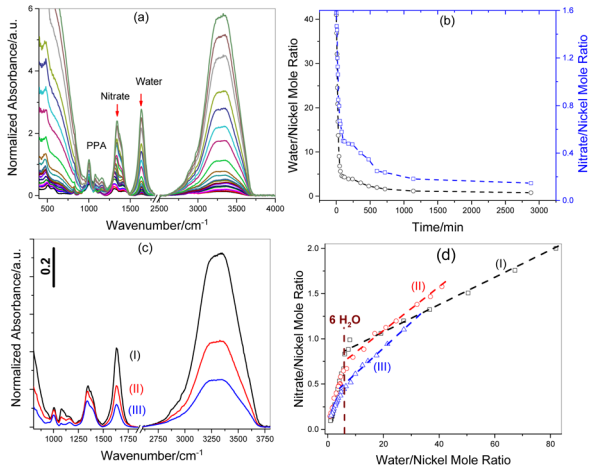

Fig. 3 (a) Normalized ATR-FTIR spectra of solution B (top to bottom, fresh, 5, 10, 15, 20, 25, 30, 40, 50, 60, 80, 100 min, 2, 3, 4, 6, 8, 10, 12, 19, and 48 h aging), (b) mole ratio of water/nickel and nitrate/nickel *versus* time of solution B (from normalized ATR-FTIR spectra of a fresh solution of B), (c) ATR-FTIR spectra of fresh samples of (I) A, (II) B, and (III) C, and (d) nitrate/nickel *versus* water/nickel mole ratio plots of solutions of (I) A, (II) B, and (III) C.

to follow quantitative changes during water evaporation (aging process). The ν-CH peak (at around 2845 cm^{-1}) of P123 or pyrophosphate peaks (at around 900–1200 cm^{-1}) are used to normalize the spectra by assuming no change in these peaks going from solution to gel phase and then later to a solid phase. Fig. 3(b), S6(a) and (b), ESI,† show the plots of normalized absorbance of the nitrate (at around 1300 cm^{-1}) and water (bending mode, at 1640 cm^{-1}) peaks for 3 different compositions, namely Ni(II) : PPA : P123 with mole ratios of 60 : 30 : 1, 30 : 15 : 1, and 90 : 45 : 1, respectively. The plots are very similar in all compositions (A, B, and C); there is a sharp drop followed by step-like decay, in accordance with the one observed in the gravimetric data. The nitrate decomposition starts in the solution phase, continues during the gelation and solidification and follows the water evaporation.

Since we know the initial composition of the drop over the ATR crystal, the first spectrum is assumed to be the spectrum of the initial solution with a known composition, see Fig. 3(c). The water-to-nickel ratio is 82, 41, and 27.3 in solutions A, B, and C, respectively. The nitrate-to-nickel ratio is assumed to be 2 in solution A. Accordingly, using the normalized spectra of fresh solutions of B and C, the nitrate/nickel mole ratio was calculated to be 1.58 and 1.10, respectively. Therefore, the absorbance data can be replotted as water/nickel and nitrate/nickel mole ratios *versus* time; see Fig. 3(d) for all 3 compositions. Solution A has the most water content and loses its water to around 6 water per nickel in a very short time (25–30 min), while the nitrate/nickel ratio drops to 0.8. Interestingly, the other more concentrated solutions, B and C, also follow a similar trend, see Fig. 3(d). There is a linear decay of nitrate amount with decreasing water in the samples during the aging process. It provides valuable information to determine the nitrate and water contents during the gelation and solidification. The plots display two regions (region I and II); region I is likely due to a gelation process with a shallow slope (due to the presence of more water), and region II is due to further polymerization of the pyrophosphate species with nickel ion, a solidification process with a deeper slope. Notice that the break-point in all three compositions is at around 6 H_2O/Ni(II), corresponding to the water coordination sphere around nickel ion, 1st shell/coordination shell. In further steps, water keeps evaporating and decaying, but water dependence on nitrate becomes more pronounced. It also means that nitrate decomposition depends on the water content of the solutions and starts in the solution phase. The nitrate/Ni(II) mole ratio drops from 2 to 0.8, while the water/Ni(II) decreases from 82 to 6 in solution A. Notice that the nitrate/Ni(II) mole ratio is 1.58 and 1.10 and H_2O/Ni(II) is 41 and 27.33 in solutions B and C, but their break-points are still at 6 H_2O/Ni(II) mole ratios. Accordingly, the spectra in the pyrophosphate region also undergo some changes due to the dissociation of PPA and coordination of dissociated PPA and Ni(II) ion, see Fig. 3(a) and eqn (1). The slope is deeper in region II, and the changes are more pronounced. The nitrate/Ni(II) and water/Ni(II) mole ratios drop down to 0.35 and 1.85 in sample A, 0.3 and 0.75 in sample B, and 0.15 and 0.7 in sample C, respectively, in 48 h. The above values are calculated using the first (fresh sample) and last (48 h aged sample) spectra and by evaluating the area under the peaks of all nitrate species and water bending regions to quantify the compositions of the aged samples. These values are slightly different from those obtained by using the intensity of the corresponding signals because the samples contain various types of nitrate species (monodentate, bidentate, and bridged coordinated species). Therefore, using the area under the curves of nitrate species and water bending mode is a more appropriate method for determining the composition of the samples. The compositions after 48 h of aging are determined to be $Ni_2H_{0.7}P_2O_7(NO_3)_{0.7}\cdot 3.7H_2O$ from solution A, $Ni_2H_{0.6}P_2O_7(NO_3)_{0.6}\cdot 1.5H_2O$ from solution B, and $Ni_2H_{0.3}P_2O_7(NO_3)_{0.3}\cdot 1.4H_2O$ from solution C. Majority of the nitrates are removed by the reaction in eqn (1) as nitric acid or its decomposition products.

The nitrate species in the $Ni_2H_xP_2O_7(NO_3)_x\cdot nH_2O$ structure are charge balancing either as free ions or coordinated to Ni^{2+} sides as a monodentate and/or bidentate ligand at room temperature (RT). Note that a free (charge balancing) nitrate appears as a single broad peak at around 1350 cm^{-1} and splits into two peaks by monodentate or bidentate coordination (due to lowering symmetry, D_{3h} to C_{2v} point groups, and splitting of the degenerate asymmetric stretching mode of nitrate) at around 1300/1409 and 1290/1470 cm^{-1}, respectively, in the IR spectrum.[42,43] Also note that a bridge-coordinated nitrate appears at 1285 and 1516 cm^{-1}.[43] Heating the samples further reduces the nitrate and water content, see Fig. 4. Fig. 4(a) and (b) show the spectral changes between RT and 100 °C. The peaks at around 1300 and 1409 cm^{-1} (with a splitting of 119 cm^{-1}, monodentate nitrate) shift to 1289 and 1506 cm^{-1} (with a splitting of 217 cm^{-1}, bridge-coordinated nitrate) by heating the sample. The water peak completely disappears at around 80 °C, indicating a complete drying of the sample and leaving mostly bridged-coordinated nitrates in the media, see Fig. 4(a) and (b). Fig. 4(c) shows the plots of x (nitrate amount)

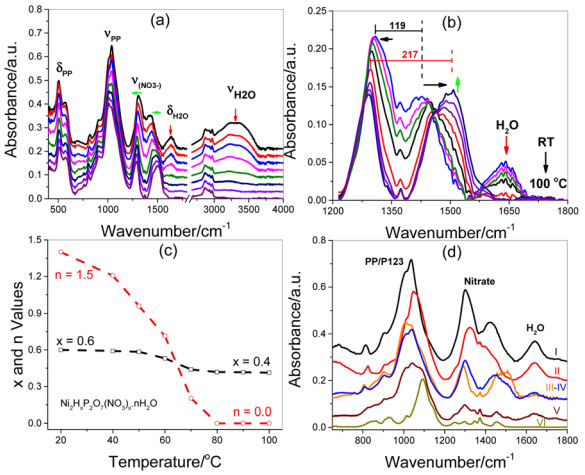

Fig. 4 ATR-FTIR data: (a) and (b) normalized spectra from solution B after 2 days of aging followed by heating at (top to bottom) RT, 40 to 100 °C with 10 °C increments, (c) the plot of x and n of $Ni_2H_xP_2O_7(NO_3)_x{\cdot}nH_2O$ *versus* temperature, and (d) spectral changes, humidity dependent changes, of 24 h aged sample under the following conditions, (I) at RT, (II) at 40 °C, (III) at 100 °C, (IV) cooled to RT, (V) 2nd cycle after exposing 85% humidity followed by heat at 100 °C then cooling to RT, and (VI) P123.

and n (water amount) values of $Ni_2H_xP_2O_7(NO_3)_x{\cdot}nH_2O$ with increasing temperature. The sample composition from solution B becomes $Ni_2H_{0.4}P_2O_7(NO_3)_{0.4}$ at 100 °C. Notice that a complete water removal from the sample stops the nitrate decomposition.

However, the nitrate content of the sample can be further reduced by exposing the fully dehydrated sample to humidity. Fig. 4(d) displays a set of ATR-FTIR spectra recorded at various conditions. Heating the sample at 40 and 100 °C reduces the nitrate concentration to a certain amount, typically around 0.2 nitrate/Ni, and they are bidentate and bridged coordinated. Suppose this sample is exposed to humidity. In that case, the water peaks reappear in the spectrum, the bridged coordinated nitrate peak loses its intensity, and the mono/bidentate coordinated nitrate peaks gain intensity. Therefore, the water molecules must be in a very close vicinity to nitrate species (if not coordinated to the same Ni(II) ion, see spectra III and IV in Fig. 4(d)) and react with each other to further reduce the nitrate content of the sample. Heating this sample first to 100 °C makes it lose its water (not shown), but cooling it back to RT reabsorbs the ambient water (see spectrum V). With this 2nd cycle of heating and cooling, the sample loses its nitrate content from 0.4 to 0.08 (namely, $Ni_2H_{0.08}P_2O_7(NO_3)_{0.08}$). Pure P123 spectrum is also given in Fig. 4(d), spectrum VI, for comparison purposes. Notice that the spectrum V, in the nitrate region, is very similar to the P123 spectrum. It means the majority of the nitrate species have been removed from the sample by this treatment. The same experiment was repeated five times, but the change in nitrate peak was minimal. Therefore, it is "impossible" to remove all nitrates and some of the protons (as $H_xP_2O_7$, –P–OH) even at 100 °C and further humidity treatment. The presence of the P–OH sides in the samples makes the product amorphous and keeps it amorphous up to 700 °C; see later. Overall, the

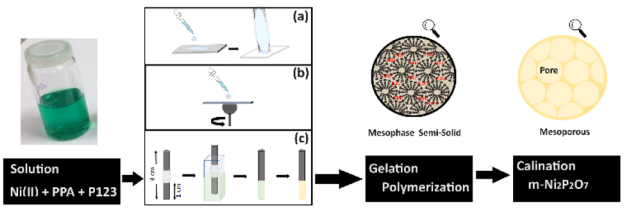

Scheme 1 Schematic representation of the synthesis and electrode fabrication process (a) drop casting, (b) spin-coating, and (c) dip coating.

synthesis process is outlined in Scheme 1. It is the transformation from a liquid crystalline (LLC) mesophase to a mesostructured semi-solid that leads to more uniform pores and offers advantages during the calcination process. This is because the mesostructured semi-solid can withstand heat treatment, unlike the salt-surfactant LLC mesophase, which melts during the calcination process, forming a disordered mesoporous metal oxide from the melted LLC phase.[44–46]

Mesoporous $Ni_2P_2O_7$ particles

Calcination of spin-, dip-coated or drop-casted samples at 300 °C produce spherical mesoporous $Ni_2P_2O_7$ particles (denoted as *m*-NiPP-*n*-X, *m* stands for mesoporous, *n* for the Ni(II)/P123 mole ratio, and *X* is the calcination temperature in Celsius). The calcined *m*-NiPP-60 sample was annealed at 400, 500, 600, and 700 °C and extensively characterized using ATR-FTIR, XRD, SEM, EDX, TEM, N_2 adsorption–desorption measurement, XPS, and electrochemical techniques.

Fig. 5(a) shows the ATR-FTIR spectra of the samples heated or calcined/annealed at various temperatures. ATR-FTIR spectra display reduced nitrate and surfactant peaks up to 200 °C; no peaks are observed from nitrate and surfactant species at 300 °

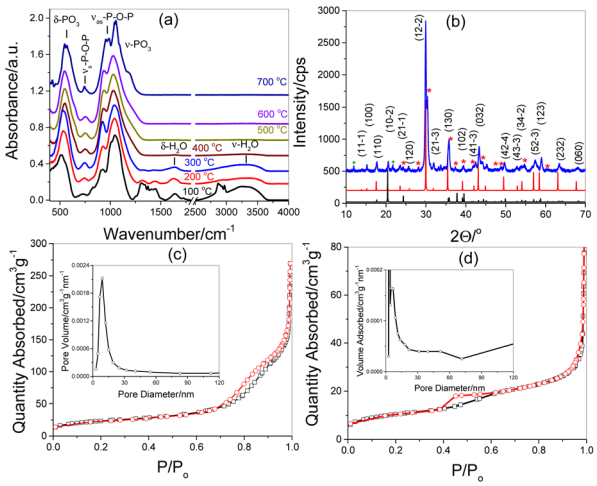

Fig. 5 ATR-FTIR spectra (a) and XRD patterns (b) of *m*-NiPP-60-700 together with α- (ICDD 00-039-0710, red) and β-$Ni_2P_2O_7$ (ICDD 04-014-1817, black) database (indexes for α-phase, red stars for β-phase and green stars for an unknown phase). N_2 (77 K) adsorption (black) and desorption (red) isotherms of (c) *m*-NiPP-30-300 and (d) *m*-NiPP-90-300 (insets are the pore size distribution plots).

C. Only peaks that remain at this temperature originate from the amorphous nickel pyrophosphate and water. The peaks at high frequency (1050–1200 cm^{-1}) correspond to PO_3 units, the peaks at around 750 and 930 cm^{-1} correspond to symmetric and asymmetric modes of the bridged P–O (P–O–P) group, and the intense peaks at around 500–600 cm^{-1} originate from the bending modes of pyrophosphate group[47] and Ni–O stretching modes, see Fig. 5(a). All the IR peaks are broad up to 700 °C, get sharper by heating at higher temperatures, and become resolved sharper peaks at 700 °C, corresponding to the crystallization of nickel pyrophosphate particles, see Fig. 5(a). The spectral features and changes show that the local pyrophosphate structure in the amorphous phase is very similar to the crystalline phase.

These samples were further characterized by using powder XRD. The diffraction pattern shows no diffraction line(s) up to 700 °C; it is amorphous and becomes crystalline at 700 °C, see Fig. 5(b) and S7, ESI.† The pattern can be indexed to a mixture of both α- and β-NiPP and a minimal amount of δ-NiPP.[48]

All three compositions were calcined at 300 °C and annealed at 400, 500, 600, and 700 °C, and their N_2 adsorption–desorption isotherms were recorded. The isotherms are type IV and characteristic of mesoporous materials; see Fig. 5(c) and 5(d).[49] Barrett–Joyner–Halenda (BJH) pore size distribution curves (from the desorption branch) of the calcined samples, prepared using solution A is relatively more uniform compared to that of the solutions B and C. Brunauer–Emmett–Teller (BET) surface area of *m*-NiPP-30-300, *m*-NiPP-60-300, and *m*-NiPP-90-300 samples are 60, 35, and 38 $m^2\ g^{-1}$, respectively. The surface area of *m*-NiPP-60-X gradually diminishes as the annealing temperature increases, primarily because the pore-walls grow at a cost of enlarging the pores. It reaches values of 31, 25, 5, and 5 $m^2\ g^{-1}$ at 400, 500, 600, and 700 °C, respectively.

The samples were further investigated by SEM and TEM imaging techniques to determine their morphology and porosity. Fig. 6 shows a set of SEM images of *m*-NiPP-60 calcined/annealed at different temperatures. The images display two distinct morphologies, namely 50–300 nm spheres and film particles; see Fig. 6 (top row) and S8.† The spherical particles are the significant component in the samples. The pores expand in size with heating and become visible in the SEM images at high temperatures. Fig. 6 (bottom row) shows the TEM images of the spherical particles of *m*-NiPP-60-300 and *m*-NiPP-60-700. Particles are perfect spheres at 300 °C but get distorted and annealed to each other at 700 °C. Fig. 6 also shows a high-resolution TEM image of *m*-NiPP-60-700. The lattice fringes are visible in the image with a lattice distance of 0.298 nm, corresponding to the (12-2) plane, which is the most intense line in the XRD pattern of alpha *m*-NiPP.

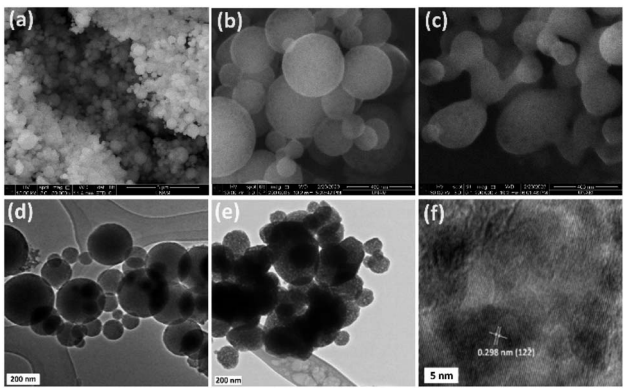

Fig. 6 SEM images of (a) *m*-NiPP-60-300 (scale bar is 3 μm), (b) *m*-NiPP-60-600 (scale bar is 400 nm), and (c) *m*-NiPP-60-700 (scale bar is 400 nm) and TEM images of (d) *m*-NiPP-60-300, (e) *m*-NiPP-60-700, and (f) HR-TEM of *m*-NiPP-60-700.

Electrochemical properties and transformation of $Ni_2P_2O_7$ to β-$Ni(OH)_2$

Above clear solutions are spin-coated over fluorine doped tin oxide (FTO) coated glasses or dip-coated over graphite rods (GR) and calcined at a desired temperature (300 to 700 °C) to obtain 1 cm^2 FTO and GR coated electrodes, denoted as FTO-NiPP-*Y*-*X* and GR-NiPP-*Y*-*X* (PP stands for pyrophosphate, *Y* is Ni/P123 mole ratio in the initial solution and *X* is calcination/annealing temperature in Celsius). Three sets of electrodes were fabricated using solutions A, B, and C, that display very similar electrochemical behaviors. Therefore, we will focus our discussion on using only electrodes obtained from solution A since it has the highest surface area. Also, dip-coated electrodes are usually much thicker than spin-coated electrodes. Therefore, the dip-coating has been carried out using five times diluted solutions. Note also that the fabricated electrodes produced using the original solution A yield particle-like species on the graphite surface, but the five times dilution ensures a smooth coating, see Fig. S9, ESI.†

Both FTO-NiPP-60-300 and GR-NiPP-30-300 electrodes were used to collect multiple cyclic voltammograms (*m*-CVs), scan rate dependent CVs, and galvanostatic charge–discharge (GCD) curves at various current densities to evaluate their

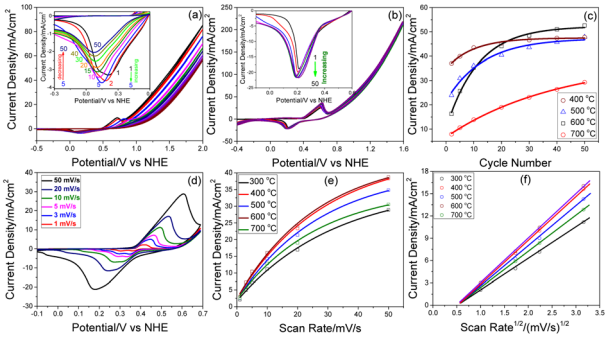

Fig. 7 Electrochemical properties of the electrodes: (a) *m*-CV of FTO-NiPP-30-300 (inset is the expanded reduction regions of *m*-CVs), (b) *m*-CV of GR-NiPP-30-300 (1st, 2nd, 5th, 10th, 20th, 30th, 40th, and 50th cycles, inset is the expanded reduction regions of *m*-CVs), (c) the current density *versus* the number of cycles using GR-NiPP-30-*X* (*X* are 400, 500, 600, and 700 °C), (d) scan rate dependent CVs (at 1, 3, 5, 10, 20, and 50 mV s^{-1} scan rates) of GR-NiPP-30-300, (e) current density (at peak maxima) *versus* scan rate plots of GR-NiPP-30-*X* (*X* of 300, 400, 500, 600, and 700), and (f) current density *versus* square root of scan rate plots of the panel (e).

electrochemical behaviours. Fig. 7(a) and (b) show *m*-CVs (collected 50 cycles at 50 mV s^{-1} scan rate) of FTO-NiPP-60-300 and GR-NiPP-30-300 electrodes in 3 M KOH solution that is a commonly used electrolyte.[20–29] Notice that the FTO-NiPP-60-300 electrode is not stable in 3 M KOH solution that the current density increases in the first 5 cycles (indicating a transformation of NiPP to $Ni(OH)_2$, see latter) and then gradually decreases (degradation of the electrode; NiPP and $Ni(OH)_2$ coating falls from the FTO surface). The reduction cycles of the *m*-CVs of the FTO-NiPP-30-300 electrode are given in Fig. 7(a) inset to illustrate its degradation in 3 M KOH solution and also because the oxidation peak overlaps with the water oxidation and makes it difficult to follow. Eventually, in further cycles, the faradaic peak disappears (not shown). Fig. S10, ESI,† displays reduction peak currents at peak maxima *versus* time plots of the FTO-NiPP-60-*X* electrodes (where *X* is 300, 400, 500, and 600). These plots clearly show that the peak current first increases and then gradually decreases over time (with an increasing number of CV cycles), indicating the transformation and degradation, respectively. Increasing the annealing temperature makes the electrodes more robust to degradation, see Fig. S10, ESI.† Note also that the initial current densities (at time zero) in the plots can be estimated using the FTO-NiPP-60-600 electrode data and the surface area of the electrodes at each annealing temperature. Because the current densities of the FTO-NiPP-60-600 electrode linearly increase in the first 10 cycles and can be fitted to evaluate the initial current density (as of 70 μA cm^{-2}) that increases to 3.74 mA cm^{-2} after 50 cycles.

However, the GR-NiPP-30 electrodes are electrochemically and mechanically more stable and used throughout all electrochemical measurements (including *m*-CVs up to 1000 cycles and GCD at all current densities). Notice that the peak current gradually increases with use and becomes stable in further cycles and other electrochemical analysis, see Fig. 7(b) (inset). Therefore, the rest of the investigations have been carried out using GR-coated electrodes. Faradaic peak, observed at around 0.6 V (*vs.* normal hydrogen electrode, NHE) in *m*-CVs at all annealing temperatures, is due to oxidation of Ni^{2+} to Ni^{3+} and maybe Ni^{3+} to Ni^{4+}.[50] A sharp increase in the current density after 0.8 V is due to water oxidation. The plots in Fig. 7(c) are the current density at oxidation peak maxima *versus* the number of CV cycles. Clearly, at all annealing temperatures, the current density of the oxidation peak gradually increases with increasing cycles or time (Fig. 7(c)). The electrode, calcined at low temperature, requires a much shorter time to reach a maximum current density, but that is much longer (or more cycles) in the electrodes annealed at higher temperatures (compare behaviours of GR-NiPP-30-400 with GR-NiPP-30-700). Notice also that the GR-NiPP-30-700 electrode also reaches a similar current density after 200 cycles and stays constant till 1000 cycles (and likely in further cycles); see Fig. S11(a) and (b), ESI.† Interestingly, the electrodes, calcined at all temperatures, perform very similarly after *m*-CVs, even though the surface area gradually decreases with increasing their annealing temperature: remember that the surface area of *m*-NiPP-30-300 is 60 m^2 g^{-1} and 5 m^2 g^{-1} in the *m*-NiPP-30-700. Therefore, it is reasonable to conclude that the amorphous electrodes (GR-NiPP-30-*X*, *X* is between 300 and 600 °C) transform very quickly to a more active form, whereas the crystalline electrode (GR-NiPP-30-700) produces the same active material in a much longer use (see latter).

The CVs were also collected at different scan rates after the electrodes became stable by *m*-CVs to ensure the change in current density was only due to the scan rate. Fig. 7(d) displays the CVs of GR-NiPP-30-300 at 6 different scan rates (namely at 1, 3, 5, 10, 20, and 50 mV s^{-1}). The scan rate dependent CVs are very similar at all other temperatures; see Fig. S12.† The current density at oxidation peak maxima *versus* scan rate and the square root of scan rate plots are shown in Fig. 7(e) and (f), respectively. The plots in Fig. 7(f) fit into straight lines, indicating a square root of scan rate dependence, meaning that the redox process is diffusion-controlled. The electrochemical reaction suggested in the literature is given in eqn (2),[25] and the behaviour observed above is consistent with this suggestion. The reaction is limited by the diffusion of hydroxide ions from the solution.

$$Ni_2P_2O_7 + 2OH^- \leftrightarrow Ni_2P_2O_7(OH)_2 + 2e^- \quad (2)$$

However, we further characterized the used *m*-NiPP electrodes to fully elucidate the origin of the above changes in the CVs by recording their EDX and XPS spectra and surprisingly found out that the phosphorus peaks in both spectra completely disappear, see Fig. S13, ESI,† and 8, respectively. Fig. 8 shows the XPS spectra in the Ni 2p, O 1s, and P 2p regions before and after *m*-CVs. The Ni 2p peaks red-shift by about 2 eV after *m*-CVs due presence of 6 two and three-coordinated oxygen atoms surrounding the Ni(II) ion in NiPP and 6 four-coordinated hydroxide ions in $Ni(OH)_2$; the O 1s peak becomes sharper, and shifts to higher binding energy (from 532.2 to 531.5 eV), but the P 2p peak completely disappears, indicating a transformation of NiPP to likely $Ni(OH)_2$ (see latter). Note also that the Ni 2p and O 1s regions are very similar to the spectra of

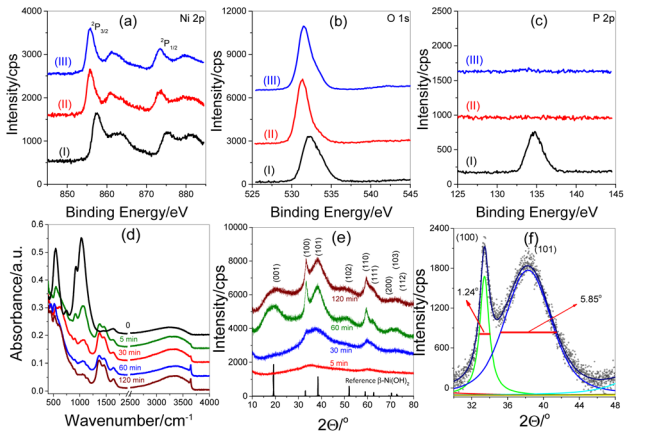

Fig. 8 XPS spectra of (I) *m*-NiPP before *m*-CVs, (II) *m*-NiPP after *m*-CVs, and (III) *m*-NiPP kept in 3 M KOH for 1 h in the (a) Ni 2p, (b) O 1s, and (c) P 2p regions. Aged samples in 3 M KOH solution for the different durations and their (d) ATR-FTIR spectra, (e) and (f) XRD patterns with ICDD card 00-059-0463 for β-$Ni(OH)_2$.

$Ni(OH)_2$ (ref. 51) after *m*-CV measurements. Moreover, the O 1s region displays a sharp peak at 531.5 eV with a shoulder on the high-energy side due to hydroxide and coordinated water.[52] We also aged the electrodes in a 3 M KOH solution for 1 h and then checked their XPS spectrum (see Fig. 8) to show that this is a chemical reaction of NiPP in a KOH solution. The spectra in all three regions are identical in both electrochemically and chemically obtained samples. Therefore, it is reasonable to suggest the following chemical equilibrium reaction (eqn (3)).

$$Ni_2P_2O_7(s) + 4OH^-(aq) \leftrightarrow 2Ni(OH)_2(s) + P_2O_7^{4-}(aq) \quad (3)$$

As a control experiment, the GR-NiPP-30-300 and GR-NiPP-30-700 electrodes were also tested by collecting their *m*-CVs in a 2.4 M KOH and 0.6 M PPA electrolyte (neutralized solution) in which all $H_4P_2O_7$ is converted to $P_2O_7^{4-}$ ion. The above electrolyte solution ensures no forward reaction, and *m*-NiPP is stable in the above electrolyte. The CVs of the electrodes display capacitive feature (between 0.0 and 1.4 V) with a faradaic peak at around 1.6 V due to oxidation of NiPP and OER at more positive potentials; no characteristic $Ni(OH)_2$ features were observed, compare Fig. S14, ESI,† 7(a) and (b). These electrodes display a 40 mA s charge capacity and 40 mF cm^{-2} specific capacitance at 2 mA cm^{-2} current density in the 0.2–1.2 V window in the neutralized electrolyte solution.

The used electrodes and large amounts of NiPP powder samples (prepared over glass slides as described above, scraped, and aged in KOH solutions) were further analysed using ATR-FTIR, XRD, and TEM imaging techniques to elucidate details of the above chemical transformation (eqn (3)). Fig. S15(a), ESI,† shows the ATR-FTIR spectra of the *m*-NiPP-300 before and after aging the sample on a microscope slide in a 3 M KOH solution and a drop of the KOH solution upon drying. Spectra of the aged and pure dried KOH samples have similar features at around 1400 cm^{-1} and originate from the same species.[53] The main peaks in the aged sample and dried KOH solution are due to $KHCO_3$ and K_2CO_3 crystals that form during drying by absorbing carbon dioxide from the ambient atmosphere. These samples also display strong diffraction lines that can be indexed to $KHCO_3$, K_2CO_3, and KOH crystals (Fig. S15(b), ESI†). Therefore, more time-dependent measurements have been carried out using samples (collected from a 3 M KOH aging solution and carefully filtered and washed with water without exposing to the ambient atmosphere) for further characterization by ATR-FTIR, XRD, and TEM techniques. Time-dependent ATR-FTIR spectra display a gradual decrease of the PP peaks (at 1030, 928, 744, and 548 cm^{-1}), an increase of peaks at 3643 cm^{-1} due to $Ni(OH)_2$ (water-free), and strongly hydrogen-bonded water and hydrated hydroxides (at 2976 and 3125, and 1645 cm^{-1}), carbonate, bicarbonate peaks (at around 1400 and 1580 cm^{-1}) and Ni–O peaks (at about 440–650 cm^{-1}), see Fig. 8(d). A similar trend is also observed in the sample annealed at 700 °C, but the change is much slower compared to the sample calcined at 300 °C. These observations correlate well with the trend in the *m*-CVs, where the current density increases with increasing cycles but much slower in the *m*-NiPP-30-700. The XRD patterns of the same samples are also collected and given in Fig. 8(e). The carefully isolated and washed samples display only very broad lines indexed to β-$Ni(OH)_2$. All the lines related to the *c*-axis are extremely broad, which means the thickness along the layer axis is only a few nanometres. However, the lines due to the (100) and (110) planes are relatively sharper. Fitting (100) and (101) provides 1.25 and 5.85° full-width half-maximum (FWHM); see Fig. 8(f). Calculation using the Scherer equation and the FWHM gives that the β-$Ni(OH)_2$ nanoparticles are 7 nm wide ($a = b =$ 3.125 Å) and 1.5 nm thick (*c*-axis, $c = 4.605$ Å).[35] This corresponds to only 3–4 layers thick and about 22-unit cell-wide particles.

The *m*-NiPP-30-300 and *m*-NiPP-30-700 samples were kept in 3 M KOH solution separately for 5 min and 1 h, and their TEM images were also collected (Fig. 9). The spherical morphology of *m*-NiPP was kept with flake-like surface features (due to $Ni(OH)_2$ particles) in the 5 min sample. After 1 h aging in the KOH solution, the particles keep the spherical morphology but are almost fully converted into β-$Ni(OH)_2$ particles as demonstrated by the ATR-FTIR spectra and XRD patterns (Fig. 9(a) and (b)). TEM image of the *m*-NiPP-30-700 sample (kept for 1 h in KOH solution) also shows annealed needle/flake-like features. Also, notice that the flake-like particles are less than 1.5 nm thick (Fig. 9(c) and (d)), as evidenced by the XRD data.

The typical weights of NiPP over 1 cm^2 FTO electrodes are 0.2, 0.3, and 0.4 mg (obtained by taking the average of 10 identical electrodes) for the FTO-NiPP-30-300, FTO-NiPP-60-300, and FTO-90-300 electrodes, respectively. However, the GR-NiPP electrodes coated by the dip-coating method are thicker and heavier. Therefore, the solution is diluted at least five times and used for the dip-coating method. More electrodes were also prepared by using more diluted solutions (namely, 5, 10, 20, and 50 times dilution) and found that there is a linear

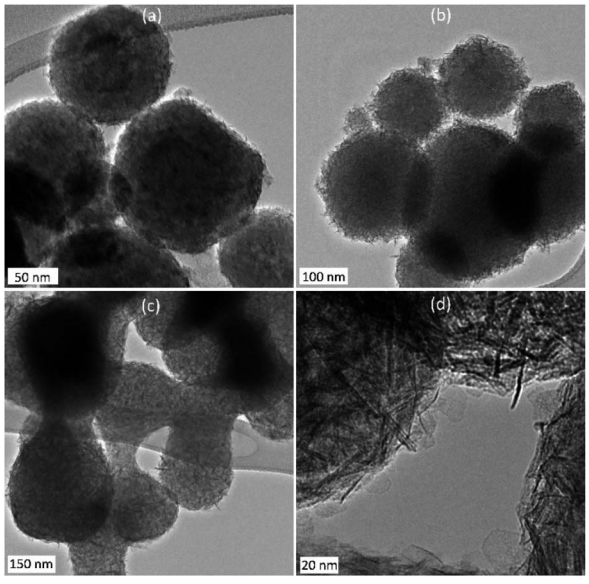

Fig. 9 TEM images of the *m*-NiPP-30-300 kept in 3 M KOH solution for (a) 5 and (b) 60 min and (c and d) *m*-NiPP-30-700 kept in 3 M KOH for 60 min.

correlation between the ln(1/ND) (ND is the number of dilutions of the original solution) or ln[Ni^{2+}] and current density, see Fig. S16.† The second plot can be used as a calibration curve to determine the relative thickness (or amount of material on GR) of the electrodes and could be used for any solution by simply measuring the current density of the electrode. Therefore, the weight of the GR-coated electrode is evaluated to be around 0.4 mg using their current densities. Also, note that a typical weight of a 1 cm^2 coated GR-NiPP-30-300 electrode coated using 5 times dilution was measured to be 0.4 mg from the average of 4 coated electrodes and consistent with the electrochemically measured value.

The fully transformed electrodes have also been used for the GCD measurements. Once more, it is crucial to mention that the electrodes, calcined at low temperatures, must be cycled for at least 50 cycles or kept in KOH solution for 1 h prior to GCD measurements. For the higher temperatures, the number of cycles must be more, typically over 200 cycles for *m*-NiPP-30-700 (until no change is observed on the CVs) to convert all NiPPs to β-$Ni(OH)_2$ particles. Fig. 10 shows the GCDs of two electrodes (calcined at 300 and 700 °C) at different current densities (1, 2, 3, 4, 5, 6, and 7 mA cm^{-2}) and their specific capacitance and capacity plots for 100 cycles. The percent coulombic efficiency is around 96–97% for all the electrodes, calcined at all temperatures, see Fig. S17.† Data for the other temperatures are tabulated in Table 1. Note also that the control experiments have been carried out using both the bared FTO and GR to determine their contribution to the charge capacity (*C*) and specific capacitance (SC) of the electrodes. The *C* and SC values are 1.7 × 10^{-3} mA s and 5.3 × 10^{-3} mF cm^{-2} (0.46 nA h cm^{-2}) for the bared FTO and 1.5 × 10^{-3} mA s and 5.0 × 10^{-2} mF cm^{-2} (4.15 nA h cm^{-2}) for the bared GR electrodes, respectively, at 1 mA cm^{-2} with a potential window of 0.3 V and negligible.

The above reaction clearly indicates that the bulk of the current is from a diffusion-limited faradaic reaction and not a capacitive event. Therefore, it is more realistic to report and compare their total charge capacity rather than specific capacitance; see Fig. S18† and the related discussion in the ESI.† We are intentionally not using the term pseudo capacitance in order to stay out of the discussion in the literature.[54] While the bulk of the current is faradaic following the reaction shown above, there is a capacitive part, albeit small. This part is simply due to the double-layer capacitance on the surface between the active material and the electrolyte. Typical capacity values vary between 102 and 177 mA s at a 1 mA cm^{-2} charging-discharging rate and do not follow any temperature-dependent trend. This is an expected result because the NiPP (amorphous or crystalline) electrodes, prepared at all temperatures, are converted to similar β-$Ni(OH)_2$ particles, as characterized above. Also, notice that the capacity decreases monotonically with increasing GCD rate with a similar rate at all temperatures between 1 and 7 mA cm^{-2}; see Fig. S19.†

Table 1 Specific capacitance and capacity values of the electrodes calcined at indicated temperatures of GR-NiPP-30-*X*. (CT is calcination temperature in °C, CD is current density in mA cm^{-2}, *C* is capacity in mA s, and SC is specific capacitance in mF cm^{-2})

CT	CD	1	2	3	4	5	6	7
300	*C*	102	93	85	80	76	72	69
	SC	340	309	283	266	254	240	231
400	*C*	152	144	135	128	120	113	107
	SC	507	479	450	426	401	378	356
500	*C*	142	135	131	124	119	114	110
	SC	473	450	435	415	395	379	368
600	*C*	177	167	151	136	123	113	105
	SC	590	556	504	454	410	376	350
700	*C*	122	112	101	89	79	70	62
	SC	406	372	338	297	265	234	208

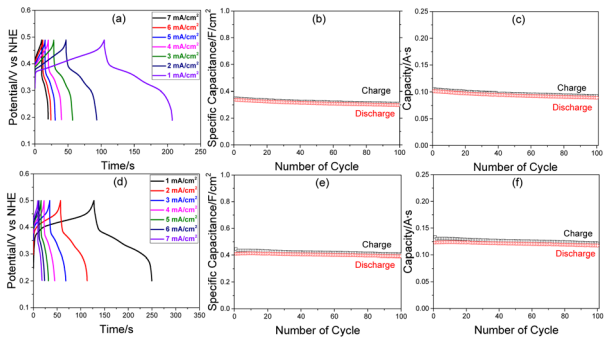

Fig. 10 Electrochemical properties: (a and d) GCD graphs, (b and e) specific capacitance *versus* the number of cycle plots, and (c and f) capacity *versus* the number of cycle plots of GR-NiPP-30-300 and GR-NiPP-30-700, respectively.

Experimental methods

Materials

Pyrophosphoric acid (PPA, ≥94%), nickel(II) nitrate hexahydrate ($[Ni(H_2O)_6](NO_3)_2$, 99.9%), poly(ethylene glycol)-*block*-poly(propylene glycol)-*block*-poly(ethylene glycol) (EO_{20}-PO_{70}-EO_{20}, pluronic P-123, Mw ∼ 5800 g mol^{-1}, 99.9%), FTO glasses, and graphite rods were purchased from the Sigma-Aldrich. All chemicals were used without further purification. Deionized water was obtained with a Millipore water purification system (18.2 MΩ cm) and used to prepare aqueous solutions.

Preparation of Ni(II) : PPA : P123 solutions

The clear solutions were prepared by dissolving $[Ni(OH_2)_6](NO_3)_2$: PPA : P123 (with *W* : *Z* : 1 mole ratio, each mole of surfactant *W* and *Z* moles of salt and acid and *W*/*Z* is stoichiometric and kept 2 to ensure $Ni_2P_2O_7$ composition) in 10 mL of deionized water. The salt/P123 mole ratio has been varied from 10 to 100 with an increment of 10; however, most works were carried out using 30, 60, and 90 mole ratios, see Table S1.†

In a typical solution preparation, nickel nitrate salt was first dissolved in 3 mL of deionized water in one vial. In another vial, surfactant and acid were dissolved in 7 mL of deionized water. Each solution was stirred for 3–4 h to ensure clear solutions, and then these two solutions were combined in one vial and stirred for another 24 h to homogenize the mixture.

Preparation of Ni(II) : PPA : P123 mesophases

Above clear solutions were coated over a glass substrate *via* either spin-coating (typically 2000 rpm for 10 s, for thin films) or drop-cast coating (for powders) methods to obtain LLC films or thicker gels, respectively. Then, these samples were used for further treatments.

Synthesis of mesoporous nickel pyrophosphates (*m*-NiPP)

Above gel-like films were directly burned at 300 °C in a preheated oven for 1 h to produce mesoporous nickel pyrophosphate (*m*-NiPP-*n*-*X*, where *n* is the salt/P123 mole ratio and *X* is the calcination or annealing temperature) and annealed at higher temperatures (400, 500, 600 and 700 °C) for 1 h in a ceramic cuvette for various characterizations. The calcined samples were collected by scraping from glass slides as powders.

Preparation of *m*-NiPP coated electrodes

The electrodes for electrochemical measurements were fabricated by dip-coating the clear solutions of Ni(II) : PPA : P123 over a 1 cm^2 area of a polished graphite rod having a 3 mm diameter[55] with a pulling speed of 1.45 mm s^{-1}. Since the dip-coating method produces thicker films over the substrate, the solutions were diluted (5-, 10-, and 15-times) using deionized water from the above solutions to obtain thinner coatings. The coated graphite rods (electrodes) were aged for a few minutes under laboratory conditions to evaporate the excess solvent and then calcined directly in a preheated oven at the desired temperature (300, 400, 500, 600, and 700 °C) for 1 h. Additionally, the FTO-coated electrodes were fabricated using the same clear solutions by spin-coating method (at 2000 rpm) and calcined/annealed as the graphite electrodes.

Characterization

Polarized optical microscope (POM) images of the gel-like films were recorded using a ZEISS Axio Scope A1 polarizing optical microscope. The small angle (1–5°) XRD patterns of the gel-like films, prepared over a glass slide, were collected using a Rigaku Miniflex diffractometer equipped with a Cu K_α ($\lambda = 1.5405$ Å) x-rays source, operating at 30 kV/15 mA and a Scintillator NaI (T1) detector with a Be window. For the wide angle (10–80°) XRD measurements, a Panalytical Multipurpose X-ray diffractometer, equipped with a CuK_α ($\lambda = 1.5405$ Å) X-rays source, operating at 45 kV/40 mA, was used from the calcined powders. The ATR-FTIR spectra were recorded with a resolution of 4 cm^{-1} and 64 scans in the 400–4000 cm^{-1} range using a Bruker Alpha Platinum ATR-IR spectrometer with a Digi Tect TM DLATGS detector. The spectra were collected by placing a few drops of the clear solutions for the gel phase analysis and a pinch of powder for the calcined samples on the diamond ATR crystal. The SEM images were recorded using an FEI Quanta 200 F scanning electron microscope on aluminium sample holders by attaching the samples using carbon tape. An FEI Technai G2 F30 microscope, at an operating voltage of 200 kV, was used to collect the transmittance electron microscope (TEM) images. The calcined films were scraped from the glass substrate, ground well in a mortar, and dispersed in absolute ethanol using a sonicator for 30 min. Then, a few drops of the dispersed solution were put on a TEM grid and heated under a powerful lamp to dry the drops quickly and to keep the particles dispersed on the grid. A Micromeritics Tristar 3000 automated gas adsorption analyser, in a relative pressure range p/p_0, from 0.01 to 0.99 over 5 min intervals, was used for the N_2 adsorption–desorption (77.4 K) measurements. The powder samples calcined at various temperatures were dehydrated at 200 °C under vacuum until the pressure in the sample tube reached 35–40 mTorr (for 2 h) before measurement. A Thermo Scientific K-α X-ray photoelectron spectrometer, operating with an Al Kα micro-focused monochromatic source (1486.68 eV and 400 μm spot size) along with a flood gun for charge neutralization, was used to record the XPS spectra using samples, scraped from glass substrate and put on a copper tape. The spectra were calibrated using the C 1s peak to 284.5 eV. The XPS spectra of the graphite electrode surface were also recorded by directly inserting the graphite-coated films into the spectrometer and making contact between the electrode surface and the spectrometer holder.

Electrochemical characterization

All electrochemical studies were carried out using a three-electrode cell; a Pt wire counter electrode, Ag/AgCl (3.5 M KCl) reference electrode, and a graphite rod coated electrodes as working electrode (coated with *m*-NiPP) were used in a polypropylene cell with a 30 mL 3.0 M KOH solution. The electrochemical measurements were carried out using a Gamry instrument (potentiostat-IFC5000-07565). The measured potentials were corrected and reported with respect to the normal hydrogen electrode (NHE). The cyclic voltammetry (CV) and galvanostatic charge/discharge (GCD) tests were subsequently recorded for each electrode on the electrochemical workstation. CV curves of the *m*-NiPP electrodes were recorded in the potential range of −0.5 to 1.5 V (*vs.* Ag/AgCl) with a scan rate of 50 mV s^{-1}. GCD was performed between 1 and 7 mA cm^{-2} of current densities with the potential limits 0.1 and 0.4 *vs.* Ag/AgCl. The specific capacitance was evaluated by analyzing galvanostatic discharge curves using the equation:[40] $C_{sc} = (I\Delta t)/(A\Delta V)$, where C_{sc} is the specific capacitance, I is the discharge current in A, Δt is the discharge time in s, A is the geometric area of coated material in cm^2, and ΔV is the difference between the potential limits in V.

Conclusions

A clear aqueous solution of Ni(II), PPA, and P123 (with Ni(II)/P123 ratios ranging from 10 to 100 and Ni(II)/PPA ratio of 2) can be coated to a substrate to create an organized mesostructured semi-solid polymeric $Ni_2H_xP_2O_7(NO_3)_x \cdot nH_2O$ (x and *n* can be as low as 0.3 and 1.4) film. The polymerization initiates in the solution phase, enhances throughout the gelation (water evaporation), and terminates with complete water evaporation from the media. Heating the same composition at just 60 °C in

a humidity chamber effectively removes nearly all nitrates from the samples. Nitrate degradation depends on water proximity to nitrate species.

Calcination of mesostructured $Ni_2H_xP_2O_7(NO_3)_x \cdot nH_2O$ yields amorphous spherical *m*-NiPP particles that crystallize into α-, some β-, and a trace of δ-NiPP phases above 700 °C. While the FTO-coated electrodes are unstable, the GR-*m*-NiPP electrodes exhibit robustness for all electrochemical tests, including stability and GCD measurements for hours. The amorphous samples show a transient current increase within the first 50 CV cycles, but the process continues up to 200 cycles in the crystalline ones at 50 mV s^{-1} scan rate. This transformation involves NiPP converting to β-$Ni(OH)_2$, retaining the spherical morphology but consisting of 1.5 nm thick, 7 nm wide flake-like β-$Ni(OH)_2$ nanoparticles. Scan rate-dependent CVs indicate a diffusion-controlled redox process, leading to $Ni(OH)_2$ transforming into NiOOH and possibly NiO_2 during oxidation. Charge capacity varies between 102 and 177 mC cm^{-2} and specific capacitance between 340 and 590 mF cm^{-2} in approximately 0.4 mg NiPP electrodes, regardless of annealing temperature or crystallinity. The GCD cycles are relatively fast, and the electrodes keep their about 94% charge capacity at 1 mA cm^{-2} (corresponds to about 6 A g^{-1}) and 77% at 7 mA cm^{-2} (corresponds to 42 A g^{-1}). Despite a surface area decrease from 60 m^2 g^{-1} to 5 m^2 g^{-1} upon annealing from 300 to 700 °C, the charge capacity and specific capacitance remain stable. This study can be extended to other metal pyrophosphates and MOFs with +2 transition metal ions for double hydroxide capacitors and batteries.

Conflicts of interest

There are no conflicts to declare.

Acknowledgements

The authors thank to TÜBİTAK (under Project 119Z877) for the financial support of this work. Ö. D. is a member of the Science Academy, Istanbul, Turkey.

Notes and references

1 F. Omenya, N. A. Chernova, R. Zhang, J. Fang, Y. Huang, F. Cohen, N. Dobryznski, S. Senanayeka, W. Xu and M. S. Whittingham, *Chem. Mater.*, 2013, **25**, 85.
2 A. K. Padhi, K. S. Nanjundaswamy and J. B. Goodenough, *J. Electrochem. Soc.*, 1997, **144**, 1188.
3 M. Pramanik, Y. Tsujimoto, V. Malgras, S. X. Dou, J. H. Kim and Y. Yamauchi, *Chem. Mater.*, 2015, **27**, 1082.
4 J. Quin, M. Zhou, Y. Cao, X. Ai and H. J. Yang, *J. Phys. Chem. C*, 2010, **114**, 3477.
5 D. B. Ranvsbaek, K. Xiang, W. Xing, O. Borkiewicz, K. M. Wiaderek, P. Gionet, K. W. Chapman, P. J. Chupas and Y. M. Chiang, *Nano Lett.*, 2014, **14**, 1484.
6 C. Sun, S. Rajasekhara, J. B. Goodenough and F. Zhou, *J. Am. Chem. Soc.*, 2011, **133**, 2132.
7 N. Zhang, C. Chen, Y. Chen, G. Chen, C. Liao, B. Liang, J. Zhang, A. Li, B. Yang, Z. Zheng, X. Liu, A. Pan, S. Liang and R. Ma, *ACS Appl. Energy Mater.*, 2018, **1**, 2016.
8 Z. Khan, B. Senthilkumar, S. Lim, R. Shanker, Y. Kim and H. Ko, *Adv. Mater. Interfaces*, 2017, **4**, 1700059.
9 C. Masquelier and L. Croguennec, *Chem. Rev.*, 2013, **113**, 6552.
10 S. Surendran, A. Sivanantham, S. Shanmugam, U. Sim and R. K. Selvan, *Sustainable Energy Fuels*, 2019, **3**, 2435.
11 H. Pang, Y. Z. Zhang, Z. Run, W. Y. Lai and W. Huang, *Nano Energy*, 2015, **17**, 339.
12 N. R. Chodankar, D. P. Dubal, S.-H. Ji and S.-H. Kim, *Small*, 2019, **99633**, 1901145.
13 B. Tain, X. Liu, B. Tu, C. Yu, J. Fan, L. Wang, Z. Xie, G. D. Stucky and D. Zhao, *Nature Mater.*, 2003, **2**, 159.
14 D. Yang, Z. Lu, X. Rui, X. Huang, H. Li, J. Zhu, W. Zhang, M. Y. Lam, H. H. Hng, H. Zhang and Q. Yan, *Angew. Chem., Inter. Ed.*, 2014, **53**, 9352.
15 C. Wei, C. Cheng, S. Wang, Y. Xu, J. Wang and H. Pang, *Chem.–Asian J.*, 2015, **10**, 1731.
16 X. Z. Lin, Z. Z. Yang, L. N. He and Z. Y. Yuan, *Green Chem.*, 2015, **17**, 795.
17 P. Mei, Y. V. Kaneti, M. Pramanik, T. Takei, Ö. Dag, Y. Sugahara and Y. Yamauchi, *Nano Energy*, 2018, **52**, 336.
18 E. Tunkara and Ö. Dag, *Eur. J. Inorg. Chem.*, 2016, **13-14**, 2114.
19 I. Uzunok, J. Kim, T. O. Çolak, D. S. Kim, H. Kim, M. Kim, Y. Yamauchi and Ö. Dag, *ChemPlusChem*, 2019, **84**, 1544.
20 F. Zhang, Y. Bao, S. Ma, L. Liu and X. Shi, *J. Mater. Chem. A*, 2017, **10**, 1.
21 A. A. Kulkarni, V. A. Savekar, T. S. Bhat and P. S. Patil, *J. Energy Storage*, 2022, **52**, 104986.
22 Y. Zhou, C. Liu, X. Li, L. Sun, D. Wu, J. Li, P. Huo and H. Wang, *J. Alloys Compd.*, 2019, **790**, 36.
23 S. J. Marje, P. K. Katkar, S. S. Pujari, S. A. Khalate, A. C. Lokhande and U. M. Patil, *Synth. Met.*, 2020, **259**, 116224.
24 K. V. Sankar, Y. Seo, S. C. Lee and S. C. Jun, *ACS Appl. Mater. Interfaces*, 2015, **10**, 8045.
25 B. Senthilkumar, Z. Khan, S. Park, K. Kim, H. Ko and Y. Kim, *J. Mater. Chem. A*, 2015, **3**, 21553.
26 Y. Yang, B. Wang, J. Zhu, J. Zhou, Z. Xu, L. Fan, J. Zhu, R. Podila, A. M. Rao and B. Lu, *ACS Nano*, 2016, **10**, 5516.
27 L. Hou, L. Lian, D. Li, J. Lin, G. Pan, L. Zhang, X. Zhang, Q. Zhanga and C. Yuan, *RSC Adv.*, 2013, **3**, 21558.
28 P. Matheswaran, P. Karuppiah, S.-M. Chen, P. Thangavelu and B. Ganapathi, *ACS Omega*, 2018, **3**, 18694.
29 B. Li, P. Gu, Y. Feng, G. Zhang, K. Huang, H. Xue and H. Pang, *Adv. Funct. Mater.*, 2017, **27**, 1605784.
30 D. Shao, Q. Wang, X. Yao, Y. Zhou and X.-Y. Yu, *J. Mater. Chem. A*, 2022, **10**, 21848.
31 H. Kim, W. Lee, W. Choi, S. Yun, E. Lee and W.-S. Yoon, *Adv. Funct. Mater.*, 2022, **32**, 2110828.
32 S. Natarajan, M. Ulaganathan and V. Aravindan, *J. Mater. Chem. A*, 2021, **9**, 15542.
33 X. Yi, H. Sun, N. Robertson and C. Kirk, *Sustainable Energy Fuels*, 2021, **5**, 5236.

34 J. Yan, Z. Fan, W. Sun, G. Ning, T. Wei, Q. Zhang, R. Zhang, L. Zhi and F. Wei, *Adv. Funct. Mater.*, 2012, **22**, 2632.
35 D. S. Hall, D. J. Lockwood, C. Bock and B. R. MacDougall, *Proc. R. Soc. A*, 2014, **471**, 20140792.
36 L. Zhang, J. Wang, J. Zhu, X. Zhang, K. S. Hui and K. N. Hui, *J. Mater. Chem. A*, 2013, **1**, 9046.
37 L. Zhang, R. Chen, K. N. Hui, K. S. Hui and H. Lee, *Chem. Eng. J.*, 2017, **325**, 554.
38 L. Li, K. S. Hui, K. N. Hui and Y. R. Cho, *J. Mater. Chem. A*, 2017, **5**, 19687.
39 Z. Tang, C. H. Tang and H. Gong, *Adv. Funct. Mater.*, 2012, **22**, 1272.
40 Z. Yu, L. Tetard, L. Zhai and J. Thomas, *Energy Environ. Sci.*, 2015, **8**, 702.
41 M. R. Querry, B. Curnette and D. William, *J. Opt. Soc. Am.*, 1969, **59**, 1299.
42 Ö. Dag, O. Samarskaya, C. Tura, A. Günay and Ö. Çelik, *Langmuir*, 2003, **19**, 3671.
43 M. Y. Mihaylov, V. R. Zdravkova, E. Z. Ivanova, H. A. Aleksandrov, P. S. Petkov, G. N. Vayssilov and K. I. Hadjiivanov, *J. Catal.*, 2021, **394**, 245.
44 G. Saat, F. M. Balci, E. P. Alsaç, F. Karadaş and Ö. Dag, *Small*, 2018, **14**, 1701913.
45 F. M. Balci, I. Karakaya, E. P. Alsaç, M. Y. Yaman, G. Saat, F. Karadaş, B. Ülgüt and Ö. Dag, *J. Mater. Chem. A*, 2018, **6**, 13925.
46 A. Amirzhanova, N. Akmansen, I. Karakaya and Ö. Dag, *ACS Appl. Energy Mater.*, 2021, **4**, 2769.
47 N. Khay, A. Ennaciri and M. Harcharras, *Vib. Spectrosc.*, 2001, **27**, 119.
48 A. G. Meguerdichian, T. Jafari, Md. R. Shakil, R. Miao, L. A. Achola, J. Macharia, A. Shirazi-Amin and S. L. Suib, *Inorg. Chem.*, 2018, **57**(4), 1815.
49 M. Thommas, *Chem. Ing. Tech.*, 2010, **82**, 1059.
50 A. Amirzhanova, I. Karakaya, C. B. Uzundal, G. Karaoğlu, F. Karadas and B. Ülgüt, *J. Mater. Chem. A*, 2019, **7**, 22012.
51 A. P. Grosvenor, M. C. Biesinger, R. C. Smart and N. S. McIntyre, *Surface Sci*, 2006, **600**, 1771.
52 J.-C. Dupin, D. Gonbeau, P. Vinatier and A. Levasseur, *Phys. Chem. Chem. Phys.*, 2000, **2**, 1319.
53 W. W. Rudolph, D. Fischer and G. Irmer, *Appl. Spectrosc.*, 2006, **60**, 130.
54 C. Constentin and J.-M. Saveant, *Chem. Sci.*, 2019, **10**, 5656.
55 N. Elgrishi, K. J. Rountree, B. D. McCarthy, E. S. Rountree, T. T. Eisenhart and J. L. A. Dempsey, *J. Chem. Educ.*, 2018, **95**, 197.